Flux-dependent occupations and occupation difference in geometrically symmetric and energy degenerate double-dot Aharonov-Bohm interferometers

Salil Bedkihal,[1] Malay Bandyopadhyay,[2] and Dvira Segal[1]

[1]*Chemical Physics Theory Group, Department of Chemistry, University of Toronto, 80 Saint George St., Toronto, Ontario, Canada M5S 3H6*
[2]*School of Basic Sciences, Indian Institute of Technology, Bhubaneswar 751007, India*
(Received 26 October 2012; revised manuscript received 31 December 2012; published 17 January 2013)

We study the steady-state characteristics and the transient behavior of the nonequilibrium double-dot Aharonov-Bohm interferometer using analytical tools and numerical simulations. Our simple setup includes noninteracting degenerate quantum dots that are coupled to two biased metallic leads at the same strength. A magnetic flux Φ pierces the interferometer perpendicularly. As we tune the degenerate dot energies away from the symmetric point, we observe four nontrivial magnetic flux-control effects: (i) flux dependency of the occupation of the dots, (ii) magnetic-flux-induced occupation difference between the dots, at degeneracy, (iii) the effect of "phase localization" of the dots' coherence holds only at the symmetric point, while in general both real and imaginary parts of the coherence are nonzero, and (iv) coherent evolution survives even when the dephasing strength, introduced via Büttiker probes, is large and comparable to the dot energies and the bias voltage. In fact, finite dephasing can actually introduce new types of coherent oscillations into the system dynamics. These four phenomena take place when the dot energies are gated, to be positioned away from the symmetric point, demonstrating that the combination of bias voltage, magnetic flux, and gating field can provide delicate control over the occupation of each of the quantum dots and their coherence.

I. INTRODUCTION

The steady-state properties of the Aharonov-Bohm (AB) interferometer have been intensively investigated,[1,2] with the motivation to explore coherence effects in electron transmission within mesoscopic and nanoscale structures.[3,4] Particularly, the role of electron-electron (e-e) interaction effects in AB interferometry has been considered in Refs. 5–12, revealing, e.g., asymmetric interference patterns[5] and the enhancement[10] or elimination[12] of the Kondo physics. Recent works further considered the possibility of magnetic-field control in molecular transport junctions.[13–16] The real-time dynamics of AB interferometers has been of recent interest, motivated by the challenge to understand quantum dynamics, particularly decoherence and dissipation, in open nonequilibrium quantum systems. Studies of electron dynamics in double-dot AB interferometers in the absence of e-e interactions have been carried out in Refs. 17–19, using a non-Markovian master-equation approach. The role of e-e repulsion effects on the dots dynamics was studied numerically using a nonperturbative method in Ref. 20.

In this paper, we focus on a simple minimal model, the biased, noninteracting double-quantum-dot AB interferometer, and study its transient and steady-state characteristics. For a scheme of this model, see Fig. 1. This system has revealed a wealth of intricate behavior, such as "flux-dependent level attraction,"[21] and the ability to achieve decoherence control when junction asymmetry is incorporated.[19] Here, this noninteracting system further displays other nontrivial effects in both the transient regime and the stationary limit. While previous studies have allowed for junction asymmetry and nondegenerate dots,[18,21] we restrict ourselves to the simplest case of energy degenerate dots and symmetric dot-lead couplings. However, in our study the degenerate levels may be tuned away from the symmetric point, i.e., they do not

necessarily reside at the center of the bias window, a situation that can be reached by applying a gating field. Using exact analytic expressions and numerical simulations, we expose several nontrivial effects emerging in this gated AB model with biased leads. (i) First, occupation of the dots displays strong flux dependency. (ii) Second, not only do the occupations vary with flux, but the dots acquire unequal occupations at degeneracy. (iii) Further, we show that the effect of "phase localization"[17] appears only at the symmetric point, while when the system is gated away from that point, dot coherences can be controlled feasibly by the bias voltage.

In the stationary limit, we further study the role of dephasing effects, implemented here through a dephasing probe,[22–24] on the coherence properties of the system. Interestingly, we find that finite and substantial dephasing strength (given by the dephasing rate $\times\hbar$), at the order of the bias voltage and dot-lead hybridization, still allows for flux dependency of occupation. However, at large dephasing, the occupation-phase dependency significantly differs from the zero dephasing limit. In other words, dephasing processes may alter coherent oscillations to provide new features. The flux dependency of the occupation is fully washed out when dephasing is significantly stronger than the applied bias voltage and the dot-lead hybridization strength.

The structure of the paper is as follows. In Sec. II, we present the double-dot AB interferometer model. Section III explores the steady-state properties of the system using the nonequilibrium Green's function approach. We derive closed analytic expressions (at zero temperature) for the occupation of the dots, the coherence between the dots, and the charge current in the system. Section IV provides numerical results in the transient regime, indicating the time scale it takes for the system to reach the stationary limit and the intricate dynamics involved. Section V details the role of dephasing effects, providing analytic expressions for the occupation of the dots in
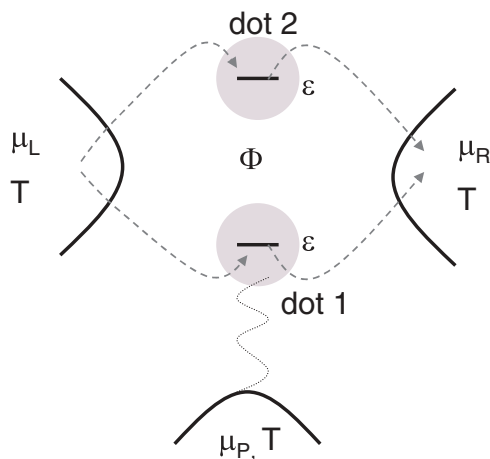
FIG. 1. Scheme of a double-dot AB interferometer. Each of the two dots is represented by a single electronic level, which do not directly couple. The total magnetic flux is denoted by Φ. Dot 1 may be susceptible to dephasing effects, introduced here through the coupling of this dot to a dephasing probe, the terminal P. The role of dephasing effects is discussed in Sec. V.

the steady-state limit. Section VI summarizes our main results and concludes.

II. MODEL

We focus on a symmetric AB setup, with a quantum dot located at each arm of the interferometer. The dots are connected to two metal leads (referred to as baths or reservoirs) maintained in a biased state. For simplicity, we do not consider here electron-electron interactions and the Zeeman effect, thus, we can ignore the spin degree of freedom and describe each quantum dot by a spinless electronic level (see Fig. 1).

We neglect the Coulomb term in order to construct a simple solvable setup showing nontrivial results to single out the effect of the threading magnetic flux on the transport behavior. The resulting analytic expressions allow us to deduce the role of bias voltage, magnetic flux, and the dot energetics on the observed characteristics. At the mean-field (Hartree) level, e-e interaction effects are contained within energy shifts, thus we expect our main observations to hold. Beyond that, we found in related studies that e-e interactions with a strength of one to four times the hybridization strength do not fundamentally alter results from related noninteracting e-e models.[20] We ignore the Zeeman level splitting since the magnetic flux is threading between the dots and not the surface of the AB ring. The total Hamiltonian H is given by

$$H = H_S + H_B + H_{SB}. \tag{1}$$

Here, H_S is the Hamiltonian for the dots (the "subsystem"), H_B includes the two metals, and H_{SB} incorporates subsystem-bath hybridization terms. Specifically, we assume uncoupled dots

$$H_S = \epsilon_1 a_1^\dagger a_1 + \epsilon_2 a_2^\dagger a_2. \tag{2}$$

To keep our discussion general, we allow the states to be nondegenerate at this point. In our analytic and numerical calculations below, we have forced degeneracy. $a_\beta^\dagger$ and a_β are the subsystem creation and annihilation operators, respectively,

where $\beta = 1, 2$. The metals are composed of noninteracting electrons

$$H_B = \sum_l \omega_l a_l^\dagger a_l + \sum_r \omega_r a_r^\dagger a_r, \tag{3}$$

where $a_{l,r}^\dagger$ and $a_{l,r}$ are bath creation and annihilation operators, for the left ($l \in L$) and right ($r \in R$) leads. The subsystem-bath hybridization term is given by

$$H_{SB} = \sum_{\beta,l} \xi_{\beta,l} a_\beta^\dagger a_l e^{i\phi_\beta^L} + \sum_{\beta,r} \zeta_{\beta,r} a_r^\dagger a_\beta e^{i\phi_\beta^R} + \text{H.c.}, \tag{4}$$

where ξ is the coupling strength to the left bath and similarly ζ stands for the coupling strength to the right bath. The notation here is general, but we later take these couplings to be identical since we are interested in a dot-lead symmetric setup. Here, ϕ_β^L and ϕ_β^R are the AB phase factors, acquired by electron waves in a magnetic field perpendicular to the device plane. These phases are constrained to satisfy the following relation:

$$\phi_1^L - \phi_2^L + \phi_1^R - \phi_2^R = \phi = 2\pi \Phi/\Phi_0, \tag{5}$$

where Φ is the magnetic flux enclosed by the ring and $\Phi_0 = hc/e$ is the flux quantum. In what follows, we adopt the gauge $\phi_1^L - \phi_2^L = \phi_1^R - \phi_2^R = \phi/2$. It can be proved that transient dynamics and steady-state characteristics of physical observables (current, occupation, and coherences) are gauge invariant.[18]

We voltage-bias the system, using the convention $\Delta\mu \equiv \mu_L - \mu_R \geqslant 0$, with $\mu_{L,R}$ as the chemical potential of the metals. While we bias the system in a symmetric manner, $\mu_L = -\mu_R$, the levels of the dots may be placed away from the so-called symmetric point at which $\mu_L - \epsilon_\beta = \epsilon_\beta - \mu_R$. This situation may be achieved by applying a gate voltage to each dot. For simplicity, we use the conventions $\hbar \equiv 1$, electron charge $e \equiv 1$, and Boltzmann constant $k_B \equiv 1$.

III. STATIONARY BEHAVIOR

A. Method: Equations of motion

Since the model is noninteracting, its steady-state characteristics can be calculated exactly using the nonequilibrium Green's function (NEGF) approach.[25] This technique has been extensively used in the past for studying transport properties in mesoscopic systems and molecular junctions.[26] We review here the steps involved so as to carefully contain the phase factors. The derivation presented here follows an equation-of-motion approach.[27] In this method, an effective quantum Langevin equation for the subsystem is obtained by solving the Heisenberg equations of motion (EOM) for the bath variables, then substituting them back into the EOM for the subsystem (dot) variables. The indices $\alpha, \beta = 1, 2$ identify the two dots. The resulting EOM is

$$
\begin{aligned}
\frac{da_\beta}{dt} = {} & -i\epsilon_\beta a_\beta - i\eta_\beta^L - i\eta_\beta^R \\
& - i \int_{t_0}^t d\tau \sum_{\alpha,l} \xi_{\beta,l} g_l^+(t-\tau) \xi_{\alpha,l}^* e^{i(\phi_\beta^L - \phi_\alpha^L)} a_\alpha(\tau) \\
& - i \int_{t_0}^t d\tau \sum_{\alpha,r} \zeta_{\beta,r}^* g_r^+(t-\tau) \zeta_{\alpha,r} e^{i(\phi_\alpha^R - \phi_\beta^R)} a_\alpha(\tau). \tag{6}
\end{aligned}
$$

The Green's functions of the (isolated) reservoirs are given by

$$g_l^+(t) = -ie^{-i\omega_l t}\theta(t), \quad g_r^+(t) = -ie^{-i\omega_r t}\theta(t). \quad (7)$$

The terms η_β^L and η_β^R are referred to as *noise*, induced on the subsystem from the left and right reservoirs, respectively. Their explicit form is

$$\eta_\beta^L = i\sum_l \xi_{\beta,l} g_l^+(t-t_0)a_l(t_0)e^{i\phi_\beta^L},$$

$$\eta_\beta^R = i\sum_r \zeta_{\beta,r}^* g_r^+(t-t_0)a_r(t_0)e^{-i\phi_\beta^R}. \quad (8)$$

As an initial condition, we take a factorized state for the total density matrix $\rho_T(t_0) = \rho_L \otimes \rho_R \otimes \rho(t_0)$, with empty dots and the reservoirs prepared in a grand canonical state $\rho_\nu = \frac{e^{-(H_\nu - \mu_\nu N)/T_\nu}}{\text{Tr}[\rho_\nu]}$, T_ν is the temperature of the $\nu = L, R$ Fermi sea, and μ_ν stands for its chemical potential. The reduced density matrix ρ denotes the state of the subsystem. Using this initial condition, noise correlations satisfy

$$\langle \eta_\beta^{\dagger L}(t)\eta_{\beta'}^L(\tau)\rangle = \sum_l \xi_{\beta,l}^* e^{i\omega_l(t-\tau)}\xi_{\beta',l}e^{-i(\phi_\beta^L - \phi_{\beta'}^L)}f_L(\omega_l),$$

$$\langle \eta_\beta^{\dagger R}(t)\eta_{\beta'}^R(\tau)\rangle = \sum_r \zeta_{\beta,r}e^{i\omega_r(t-\tau)}\zeta_{\beta',r}^* e^{i(\phi_\beta^R - \phi_{\beta'}^R)}f_R(\omega_r),$$

with the Fermi function $f_\nu(\omega) = [e^{(\omega-\mu_\nu)/T_\nu}+1]^{-1}$ and the expectation values evaluated in the Heisenberg representation $\langle A(t)\rangle = \text{Tr}_T[\rho_T(t_0)A(t)]$, tracing over all degrees of freedom. Steady-state properties are reached by taking the limits $t_0 \to -\infty$ and $t \to \infty$. We now Fourier transform Eq. (6) using the convolution theorem with the convention $\tilde{a}_\beta(\omega) = \int_{-\infty}^\infty dt\, a_\beta(t)e^{i\omega t}$, $\tilde{\eta}_\beta(\omega) = \int_{-\infty}^\infty dt\, \eta_\beta(t)e^{i\omega t}$. The result, organized in a matrix form, is

$$\tilde{a}_\beta(\omega) = \sum_\alpha G_{\beta,\alpha}^+\left[\tilde{\eta}_\alpha^L(\omega) + \tilde{\eta}_\alpha^R(\omega)\right], \quad (9)$$

with the Green's function

$$G_{\beta,\alpha}^+(\omega) = \frac{1}{(\omega-\epsilon_\beta)\delta_{\alpha,\beta} - \Sigma_{\beta,\alpha}^{L,+}(\omega) - \Sigma_{\beta,\alpha}^{R,+}(\omega)}. \quad (10)$$

The self-energies contain the phase factors

$$\Sigma_{\beta,\alpha}^{L,+}(\omega) = \sum_l \xi_{\beta,l}g_l^+(\omega)\xi_{\alpha,l}^* e^{i(\phi_\beta^L - \phi_\alpha^L)},$$

$$\Sigma_{\beta,\alpha}^{R,+}(\omega) = \sum_r \zeta_{\beta,r}^* g_r^+(\omega)\zeta_{\alpha,r}e^{i(\phi_\alpha^R - \phi_\beta^R)}. \quad (11)$$

We also define the conjugated-transposed matrix $G^- = (G^+)^\dagger$, to be used in the following. The real part of the self-energy is a principal value integral, which vanishes when the metals' density of states is energy independent and the bandwidth is large. We then define the hybridization matrix from the relation $\Sigma^+ = -i\Gamma/2$:

$$\Gamma_{\beta,\beta'}^L(\omega) = 2\pi e^{i(\phi_\beta^L - \phi_{\beta'}^L)}\sum_l \xi_{\beta,l}\delta(\omega-\omega_l)\xi_{\beta',l}^*. \quad (12)$$

Similar expressions hold for the R side. Using the steady-state solution (9), we can write an expression for the reduced density matrix. Back transformed to the time domain, it takes the

form

$$\langle a_\alpha^\dagger a_\beta\rangle \equiv \rho_{\alpha,\beta} = \frac{1}{2\pi}\int_{-\infty}^\infty [(G^+\Gamma^L G^-)_{\alpha,\beta}f_L(\omega)$$

$$+ (G^+\Gamma^R G^-)_{\alpha\beta}f_R(\omega)]d\omega. \quad (13)$$

The time variable has been suppressed here since this result is only valid in the steady-state limit. In what follows, we take $\xi_{\beta,l}$ and $\zeta_{\beta,r}$ as real constants, independent of the level index and the reservoir state, resulting in

$$\Gamma_{\beta,\beta'}^L = \gamma_L e^{i(\phi_\beta^L - \phi_{\beta'}^L)}, \quad \Gamma_{\beta,\beta'}^R = \gamma_R e^{-i(\phi_\beta^R - \phi_{\beta'}^R)}, \quad (14)$$

where the coefficient γ_ν, defined through this relation and Eq. (12), is taken as a constant (energy independent). Using these definitions, the matrix G^+ takes the form

$$G^+ = \begin{bmatrix} \omega - \epsilon_1 + \frac{i(\gamma_L+\gamma_R)}{2} & \frac{i\gamma_L}{2}e^{i\phi/2} + \frac{i\gamma_R}{2}e^{-i\phi/2} \\ \frac{i\gamma_L}{2}e^{-i\phi/2} + \frac{i\gamma_R}{2}e^{i\phi/2} & \omega - \epsilon_2 + \frac{i(\gamma_L+\gamma_R)}{2} \end{bmatrix}^{-1} \quad (15)$$

and the hybridization matrices are given by

$$\Gamma^L = \gamma_L\begin{bmatrix} 1 & e^{i\phi/2} \\ e^{-i\phi/2} & 1 \end{bmatrix}, \quad \Gamma^R = \gamma_R\begin{bmatrix} 1 & e^{-i\phi/2} \\ e^{i\phi/2} & 1 \end{bmatrix}. \quad (16)$$

We can now calculate, numerically or analytically, the behavior of the reduced density matrix under different conditions.[18] Since we are only concerned here with *symmetric* dot-lead couplings, we take $\gamma_L = \gamma_R = \gamma/2$. Furthermore, we impose energy degeneracy $\epsilon_1 = \epsilon_2 = \epsilon$. This choice simplifies the relevant matrices to

$$G^+ = \begin{bmatrix} \omega - \epsilon + \frac{i\gamma}{2} & \frac{i\gamma}{2}\cos\frac{\phi}{2} \\ \frac{i\gamma}{2}\cos\frac{\phi}{2} & \omega - \epsilon + \frac{i\gamma}{2} \end{bmatrix}^{-1},$$

$$\Gamma^L = \frac{\gamma}{2}\begin{bmatrix} 1 & e^{i\phi/2} \\ e^{-i\phi/2} & 1 \end{bmatrix}, \quad \Gamma^R = \frac{\gamma}{2}\begin{bmatrix} 1 & e^{-i\phi/2} \\ e^{i\phi/2} & 1 \end{bmatrix}. \quad (17)$$

We present closed analytic expressions for the diagonal and off-diagonal elements of the reduced density matrix in Sec. III B. Complementing numerical data for the real-time dynamics are included in Sec. IV. This discussion is generalized in Sec. V to include a dephasing probe.

B. Observables

1. Occupation of the dots

We expose here two effects that persist away from the "symmetric point," defined as $\mu_L - \epsilon = \epsilon - \mu_R$: The dots' occupations significantly vary with flux, and moreover, the degenerate dots acquire different occupations. After presenting general expressions away from the symmetric point, we consider other relevant cases: the finite-bias limit at the symmetric point, the limit of infinite bias (which effectively reduces to the symmetric point), and the case of $\phi = 2\pi n$, $n = 0,1,2,\ldots$.

Analytic results are obtained from Eqs. (13) and (17). Organizing these expressions, we find that the occupation of

dot 1, $\rho_{1,1} \equiv \langle a_1^\dagger a_1 \rangle$, is given by two integrals

$$\rho_{1,1} = \frac{\gamma}{4\pi} \int_{-\infty}^{\infty} d\omega f_L(\omega) \frac{(\omega - \epsilon)^2 + \omega_0^2 - 2\omega_0(\omega - \epsilon)\cos\frac{\phi}{2}}{\left[(\omega - \epsilon)^2 - \omega_0^2\right]^2 + [\gamma(\omega - \epsilon)]^2}$$
$$+ \frac{\gamma}{4\pi} \int_{-\infty}^{\infty} d\omega f_R(\omega) \frac{(\omega - \epsilon)^2 + \omega_0^2 + 2\omega_0(\omega - \epsilon)\cos\frac{\phi}{2}}{\left[(\omega - \epsilon)^2 - \omega_0^2\right]^2 + [\gamma(\omega - \epsilon)]^2}, \tag{18}$$

where we have introduced

$$\omega_0 \equiv \frac{\gamma}{2} \sin\frac{\phi}{2}. \tag{19}$$

Similarly, the occupation of level 2, $\rho_{2,2} \equiv \langle a_2^\dagger a_2 \rangle$, is given by

$$\rho_{2,2} = \frac{\gamma}{4\pi} \int_{-\infty}^{\infty} d\omega f_L(\omega) \frac{(\omega - \epsilon)^2 + \omega_0^2 + 2\omega_0(\omega - \epsilon)\cos\frac{\phi}{2}}{\left[(\omega - \epsilon)^2 - \omega_0^2\right]^2 + [\gamma(\omega - \epsilon)]^2}$$
$$+ \frac{\gamma}{4\pi} \int_{-\infty}^{\infty} d\omega f_R(\omega) \frac{(\omega - \epsilon)^2 + \omega_0^2 - 2\omega_0(\omega - \epsilon)\cos\frac{\phi}{2}}{\left[(\omega - \epsilon)^2 - \omega_0^2\right]^2 + [\gamma(\omega - \epsilon)]^2}. \tag{20}$$

In what follows, we consider the zero-temperature limit. The Fermi functions take then the shape of step functions, and the upper limits of the integrals are replaced by the corresponding chemical potentials. We now study the contribution of the odd term in the integrand. This term is responsible for the development of occupation difference between the dots:

$$\frac{\gamma}{4\pi} \int_{\mu_R}^{\mu_L} d\omega \frac{2\omega_0(\omega - \epsilon)\cos\frac{\phi}{2}}{\left[(\omega - \epsilon)^2 - \omega_0^2\right]^2 + [\gamma(\omega - \epsilon)]^2}$$
$$= \frac{\sin\frac{\phi}{2}}{8\pi} \ln\left[\frac{F_+(\phi)}{F_-(\phi)}\right], \tag{21}$$

where the explicit form of the factors $F_\pm$ is

$$F_\pm(\phi) = \frac{\gamma^4}{8} \sin^4\frac{\phi}{2} + 2(\mu_L - \epsilon)^2(\mu_R - \epsilon)^2$$
$$+ \frac{\gamma^2}{2}\left(\cos\frac{\phi}{2} \pm 1\right)^2 (\mu_L - \epsilon)^2$$
$$+ \frac{\gamma^2}{2}\left(\cos\frac{\phi}{2} \mp 1\right)^2 (\mu_R - \epsilon)^2. \tag{22}$$

For details, see Appendix A. Since it is a sum of real quadratic terms, $F_\pm \geq 0$. Inspecting Eq. (21), we note that it vanishes in four different cases: (i) at zero bias, when $\mu_L = \mu_R = 0$, (ii) at infinite bias, $\mu_L \to \infty$ and $\mu_R \to -\infty$, (iii) at the symmetric point when $\mu_L - \epsilon = \epsilon - \mu_R$, including the case $\epsilon = 0$ and $\mu_L = -\mu_R$, or when (iv) $\phi = n\pi$, $n = 0,1,2,\ldots$ (leading to $F_+ = F_-$). Combining Eq. (21) with the integration of even terms in Eq. (18), at zero temperature, we resolve the
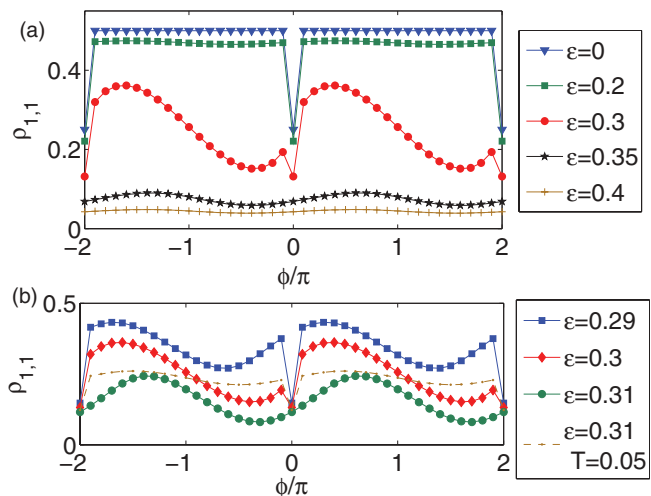
FIG. 2. (Color online) (a) Flux dependency of occupation for dot 1 using $\epsilon = 0$ (triangle), $\epsilon = 0.2$ ($\square$), $\epsilon = 0.3$ ($\circ$), $\epsilon = 0.35$ ($\star$), and $\epsilon = 0.4$ (+) for the dots' energies. Panel (b) displays results when ϵ is tuned to the edge of the bias window, $\epsilon \sim \mu_L$, $\epsilon = 0.29$ ($\square$), $\epsilon = 0.3$ (diagonal), $\epsilon = 0.31$ ($\circ$), and $\epsilon = 0.31$, $T = 0.05$ (dashed-dotted line). In all cases, $\mu_L = -\mu_R = 0.3$, $\gamma = 0.05$, and $T = 0$, unless otherwise stated.

occupations

$$\rho_{1,1/2,2} = \frac{1}{4\pi}\left[2\pi + \tan^{-1}\left(\frac{\mu_L - \epsilon}{\gamma_-}\right) + \tan^{-1}\left(\frac{\mu_L - \epsilon}{\gamma_+}\right) \right.$$
$$+ \tan^{-1}\left(\frac{\mu_R - \epsilon}{\gamma_-}\right) + \tan^{-1}\left(\frac{\mu_R - \epsilon}{\gamma_+}\right)\right]$$
$$\pm \frac{\sin\frac{\phi}{2}}{8\pi} \ln\left[\frac{F_-(\phi)}{F_+(\phi)}\right]. \tag{23}$$

The positive sign corresponds to $\rho_{1,1}$, the negative sign provides $\rho_{2,2}$. We have also introduced the notation $\gamma_\pm \equiv \frac{\gamma}{2}(1 \pm \cos\frac{\phi}{2})$. Equation (23) predicts flux dependency of electron occupation *at degeneracy*, using symmetric hybridization constants, once the dots are tuned *away* from the symmetric point. Figure 2 displays this behavior, and we find that as the dot energies get closer to the bias edge, $\epsilon \sim \mu_L$, the occupation strongly varies with ϵ [Fig. 2(b)]. It is also interesting to note that the abrupt jump at $\phi = 2\pi n$ disappears once the levels reside at or above the bias window, for $\epsilon \geq \mu_L$. This feature results from the strict zero-temperature limit assumed in the analytic calculations [a more detailed discussion follows Eq. (25)]. When the temperature is high enough, $T \sim \gamma$, the phase dependency of the occupation is washed out (see Fig. 6). The following parameters are used here and below: flat wide bands, dot energies at the order of $\epsilon = 0$–0.4, hybridization strength $\gamma = 0.05$–0.5, and zero temperature, unless otherwise specified. The bias voltage is set symmetrically around the equilibrium Fermi energy, $\mu_L = -\mu_R$, $\Delta\mu \equiv \mu_L - \mu_R$.

We now discuss in more details the behavior of the occupation in some special cases. First, we consider the symmetric point at finite bias and $\phi \neq 2\pi n$, $n = 0,1,2,\ldots$. In this case, Eq. (23) precisely reduces to

$$\rho_{\alpha,\alpha}(\mu_L - \epsilon = \epsilon - \mu_R) = \tfrac{1}{2}. \tag{24}$$

This result holds in the infinite bias limit $\mu_L \to \infty$ and $\mu_R \to -\infty$, irrespective of the (finite) value of ϵ. Next, the special case $\phi = 2\pi n$ should be separately evaluated. At these points, we have $\omega_0 = 0$ and Eq. (18) provides the simple form at zero temperature

$$\rho_{\alpha,\alpha}(\phi = 2\pi n)$$
$$= \frac{\gamma}{4\pi} \int_{-\infty}^{\mu_L - \epsilon} \frac{dx}{x^2 + \gamma^2} + \frac{\gamma}{4\pi} \int_{\epsilon - \mu_R}^{\infty} \frac{dx}{x^2 + \gamma^2}$$
$$= \frac{1}{4\pi} \left[\tan^{-1}\left(\frac{\mu_L - \epsilon}{\gamma} \right) + \tan^{-1}\left(\frac{\mu_R - \epsilon}{\gamma} \right) \right] + \frac{1}{4}. \tag{25}$$

These points are reflected by abrupt jumps in the occupation-flux behavior. Specifically, at the symmetric point, there is a sharp reduction of occupation number from $\frac{1}{2}$ [Eq. (24)] to $\frac{1}{4}$ [Eq. (25)], as observed earlier in Ref. 17. Figure 2 shows that at (strictly) zero temperature, this jump disappears once the dot energies are placed at or above the bias edge $\epsilon \geqslant \mu_L$ since resonant transmission is excluded and tunneling of electrons is the only allowed transport mechanism. At finite T, the jump at $\phi = 2\pi n$ survives even for $\epsilon > \mu_L$ due to the contribution of resonant electrons. The behavior of the dot's occupation with temperature is displayed in Fig. 6.

The total electronic occupation of the dots, at steady state, generalizes the standard symmetric case attained in Ref. 18:

$$\rho_{1,1} + \rho_{2,2} = \frac{\gamma}{2\pi} \int_{-\infty}^{\infty} d\omega \frac{[(\omega - \epsilon)^2 + \omega_0^2][f_L(\omega) + f_R(\omega)]}{[(\omega - \epsilon)^2 - \omega_0^2]^2 + [\gamma(\omega - \epsilon)]^2}. \tag{26}$$

We now highlight one of the main results of the paper: the onset of occupation difference in this degenerate ($\epsilon_1 = \epsilon_2$) and spatially symmetric ($\gamma_L = \gamma_R$) setup. Using Eq. (23), we
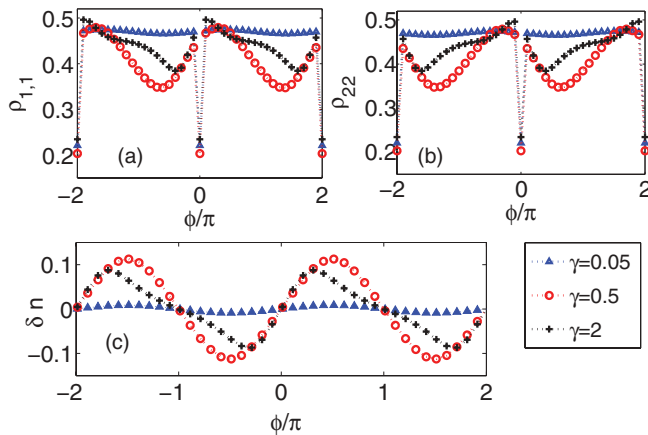
FIG. 3. (Color online) (a), (b) Occupation of the dots as a function of ϕ for $\Delta\mu = 0.6$, $\epsilon = 0.2$, $T = 0$. (c) Occupation difference $\delta n = \rho_{1,1} - \rho_{2,2}$. At weak coupling $\gamma = 0.05$ ($\triangle$), the occupation of the dots is almost identical. When the hybridization is made stronger, $\gamma = 0.5$ ($\circ$), comparable to the displacement of the levels from the symmetric point, $\rho_{1,1}$ clearly deviates from $\rho_{2,2}$. At very strong coupling $\gamma = 2$ (+), the occupation difference reduces and asymmetries develop. For clarity, results are shown for ϕ/π between $(-2,2)$.
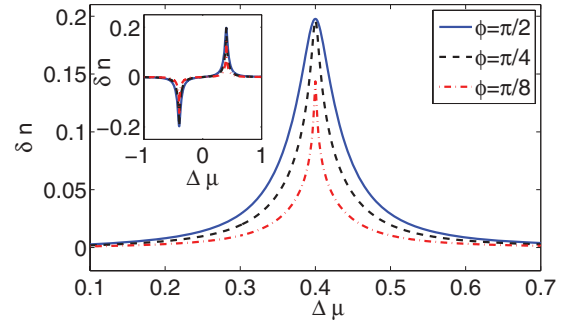
FIG. 4. (Color online) Occupation difference as a function of bias voltage $\Delta\mu$, for different phases $\phi = \pi/2$ (full line), $\phi = \pi/4$ (dashed line), $\phi = \pi/8$ (dashed-dotted line). Other parameters are $\epsilon = 0.2$ and $\gamma = 0.05$, $T = 0$. The inset presents data for backward and forward biases; the main plot zooms on the positive bias regime.

find that

$$\delta n \equiv \rho_{1,1} - \rho_{2,2} = \frac{\sin\frac{\phi}{2}}{4\pi} \ln\left[\frac{F_-(\phi)}{F_+(\phi)} \right]. \tag{27}$$

As we mentioned above, this quantity is nonzero when the following (sufficient) conditions are simultaneously satisfied: (i) the bias voltage is finite, neither zero nor infinite, (ii) the dots are positioned away from the symmetric point $\epsilon \neq (\mu_L + \mu_R)/2$, and (iii) the phase ϕ is not a multiple of π, $\phi \neq n\pi$, $n = 0, 1, 2, \ldots$. To rephrase this observation, the occupation difference can be controlled by manipulating the subsystem-metal hybridization energy γ, by changing the bias voltage, by applying a gate voltage for tuning the dot energies, and by modulating the phase ϕ through the magnetic flux. The role of these control knobs is illustrated in Figs. 3–5.

In Fig. 3, we display the level's occupation in the resonant regime $\mu_R < \epsilon < \mu_L$ while varying γ. At weak coupling, δn is insignificant. However, the occupation difference becomes large when cotunneling effects contribute. More notably, Fig. 4 illustrates the strong controllability of δn with applied voltage. We find that the occupation difference is maximized at the edge of the resonant transmission window, when $\mu_L - \epsilon = 0$ (or, equivalently, when $\Delta\mu = 2\epsilon$). The magnetic flux affects the width and height of the peak, but not the absolute position which is only determined by the offset of ϵ from the center of
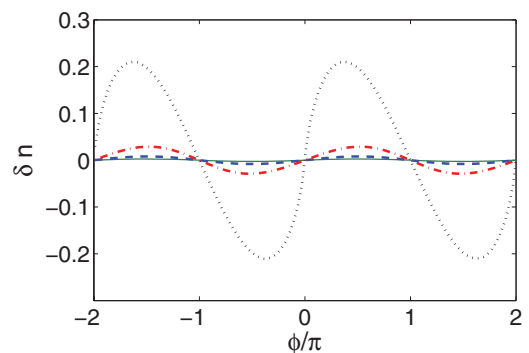
FIG. 5. (Color online) Occupation difference as a function of ϕ for different bias values $\Delta\mu = 0.1$ (full line), $\Delta\mu = 0.2$ (dashed line), $\Delta\mu = 0.3$ (dashed-dotted line), and $\Delta\mu = 0.4$ (dotted line). Other parameters are $\epsilon = 0.2$, $\gamma = 0.05$, and $T = 0$.
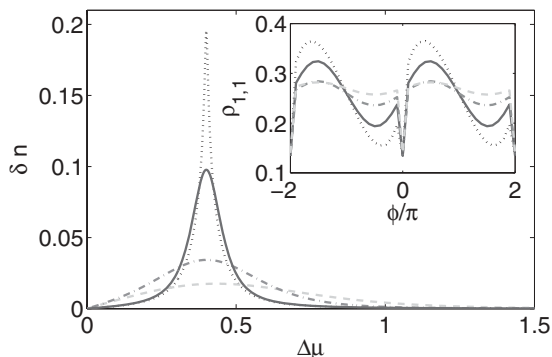
FIG. 6. Finite-temperature behavior. Main plot: Occupation difference as a function of bias voltage for $\phi = \pi/4$. Inset: Occupation of dot 1 as a function of ϕ for $\Delta\mu = 0.4$. In both panels $T = 0$ (dotted line), $T = 0.01$ (full line), $T = 0.05$ (dashed-dotted line), and $T = 0.1$ (dashed line). Dot parameters are $\epsilon = 0.2$ and $\gamma = 0.05$.

the bias window. In Fig. 5, we further show the flux dependency of δn, which is particularly significant when $\Delta\mu = 2\epsilon$.

The effect of finite temperature on the occupation-flux dependence, and on the development of occupation difference, is displayed in Fig. 6. We find that the effects largely survive

at finite T, as long as $T < \gamma$. These results were calculated numerically, based on Eqs. (18) and (20).

2. Coherence

It was recently argued that the decoherence behavior in our generic setup, including two noninteracting (uncoupled) quantum dots interferometer, can be suppressed when the device geometry is made asymmetric and nondegenerate, using $\epsilon_1 \neq \epsilon_2$ and $\gamma_L \neq \gamma_R$.[19] The requirement for asymmetry in this work arises from the observation of the "phase-localization" effect, which hinders phase manipulation in the system at the symmetric point. The term "phase localization" refers to the fact that if we define $\rho_{1,2}(t) = |\rho_{1,2}(t)|e^{i\varphi(t)}$, the relative phase φ localizes to the values $-\pi/2$ or $\pi/2$ in the long-time limit when $\phi \neq 2\pi n$, n is an integer.[17] Based on numerical simulations, we have pointed out in Ref. 20 that phase localization occurs *only* at the symmetric point, while at other values of ϵ the real part of $\rho_{1,2}$ is finite and nonzero in the asymptotic limit for any phase aside from $2\pi n$.[20] This observation is established here analytically in the steady-state limit, implying that decoherence could be suppressed in degenerate-symmetric systems once the dots are gated, with their levels shifted relative to the center of the bias window.

We derive a closed expression for the off-diagonal system element $\rho_{1,2} \equiv \langle a_1^\dagger a_2 \rangle$ by studying Eq. (13):

$$\rho_{12} = \frac{\gamma}{4\pi} \int_{-\infty}^{\infty} d\omega f_L(\omega) \left\{ \frac{\cos\frac{\phi}{2}\left[(\omega-\epsilon)^2 - \omega_0^2\right] + i\sin\frac{\phi}{2}\left[(\omega-\epsilon)^2 + \omega_0^2\right]}{\left[(\omega-\epsilon)^2 - \omega_0^2\right]^2 + \left[\gamma(\omega-\epsilon)\right]^2} \right\}$$
$$+ \frac{\gamma}{4\pi} \int_{-\infty}^{\infty} d\omega f_R(\omega) \left\{ \frac{\cos\frac{\phi}{2}\left[(\omega-\epsilon)^2 - \omega_0^2\right] - i\sin\frac{\phi}{2}\left[(\omega-\epsilon)^2 + \omega_0^2\right]}{\left[(\omega-\epsilon)^2 - \omega_0^2\right]^2 + \left[\gamma(\omega-\epsilon)\right]^2} \right\}. \tag{28}$$

At finite bias and zero temperature, direct integration provides the real (Re) and imaginary (Im) parts of $\rho_{1,2}$ ($\phi \neq 2\pi n$):

$$\mathrm{Re}\rho_{1,2} = \frac{1}{4\pi}\left[\tan^{-1}\left(\frac{\mu_L - \epsilon}{\gamma_+}\right) - \tan^{-1}\left(\frac{\mu_L - \epsilon}{\gamma_-}\right) \right.$$
$$\left. + \tan^{-1}\left(\frac{\mu_R - \epsilon}{\gamma_+}\right) - \tan^{-1}\left(\frac{\mu_R - \epsilon}{\gamma_-}\right) \right] \tag{29}$$

and

$$\mathrm{Im}\rho_{1,2} = \frac{1}{4\pi}\sin(\phi/2)\left[\tan^{-1}\left(\frac{\mu_L - \epsilon}{\gamma_+}\right) + \tan^{-1}\left(\frac{\mu_L - \epsilon}{\gamma_-}\right) \right.$$
$$\left. - \tan^{-1}\left(\frac{\mu_R - \epsilon}{\gamma_+}\right) - \tan^{-1}\left(\frac{\mu_R - \epsilon}{\gamma_-}\right) \right]. \tag{30}$$

As before, we define $\gamma_\pm = \frac{\gamma}{2}(1 \pm \cos\frac{\phi}{2})$. We now readily confirm that at the symmetric point the real part vanishes and "phase localization" takes place.[17] In particular, in the infinite bias limit we find $\mathrm{Im}\rho_{1,2} = \frac{1}{2}\sin\frac{\phi}{2}$, in agreement with previous studies.[20] We also include the behavior at the special points $\phi = 2\pi n$. Equation (28) reduces then to a simple Lorentzian

form, at zero temperature,

$$\rho_{1,2}(\phi = 0)$$
$$= \frac{\gamma}{4\pi} \int_{-\infty}^{\mu_L - \epsilon} \frac{dx}{x^2 + \gamma^2} + \frac{\gamma}{4\pi} \int_{\epsilon - \mu_R}^{\infty} \frac{dx}{x^2 + \gamma^2}$$
$$= \frac{1}{4\pi}\left[\tan^{-1}\left(\frac{\mu_L - \epsilon}{\gamma}\right) + \tan^{-1}\left(\frac{\mu_R - \epsilon}{\gamma}\right) \right] + \frac{1}{4}. \tag{31}$$

The overall sign reverses for $\phi = \pm 2\pi$. We note that the imaginary part of the coherence identically vanishes at zero phase while the real part is finite, approaching the value $\frac{1}{4}$ at the symmetric point.

Numerical results in the steady-state limit are displayed in Fig. 7. We find that both the real and imaginary parts of $\rho_{1,2}$ demonstrate significant features when the dots' levels cross the bias window at $\Delta\mu = 2\epsilon$. The value of the real part abruptly changes sign, the imaginary part develops a step. At large bias, $\mathrm{Re}\rho_{1,2}$ diminishes while $\mathrm{Im}\rho_{1,2}$ is finite, indicating on the development of the phase-localization behavior. It can be shown that the double-step structure of $\mathrm{Im}\rho_{1,2}$ (as a function of $\Delta\mu$) disappears when the dot energies are set at the symmetric point.
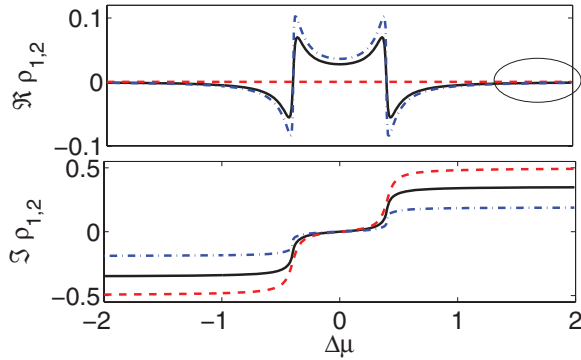
FIG. 7. (Color online) Real and imaginary parts of the coherence as a function of the bias voltage. $\phi = \pi$ (dashed line), $\phi = \pi/2$ (full line), $\phi = \pi/4$ (dashed-dotted line). Other parameters are $\epsilon = 0.2$, $\gamma = 0.05$, and $T = 0$. The oval shape marks the region of phase localization at positive bias.

3. Current

It is of interest to complement our study of subsystem (dot) properties and examine the transmission coefficient and the overall charge current in the system. The electric current, flowing from the L metal to the R end, is obtained by defining the number operator $N_L \equiv \sum_l a_l^\dagger a_l$, providing the current $J_{L \to R} = -\frac{dN_L}{dt} = -i[H, N_L]$. This yields

$$J_{L \to R} = i \sum_{l, \alpha = 1,2} \left(\xi_{\alpha,l}^* e^{-i\phi_\alpha^L} \langle a_l^\dagger a_\alpha \rangle - \xi_{\alpha,l} e^{i\phi_\alpha^L} \langle a_\alpha^\dagger a_l \rangle \right). \quad (32)$$

Expectation values are calculated in the steady-state limit. Using the EOM formalism as explained in Sec. III, we get the standard result[25]

$$J_{L \to R} = \frac{1}{2\pi} \int_{-\infty}^{\infty} d\omega \, \mathcal{T}_{LR}(\omega)[f_L(\omega) - f_R(\omega)]. \quad (33)$$

The transmission coefficient is defined as $\mathcal{T}_{LR} = \text{Tr}(\Gamma^L G^+ \Gamma^R G^-)$, where the trace is performed over the states of the subsystem (dots). In the present model, at zero temperature, we obtain

$$
\begin{aligned}
J_{L \to R} &= \frac{1}{2\pi} \int_{\mu_L}^{\mu_R} d\omega \frac{\gamma^2 (\omega - \epsilon)^2 \cos^2 \frac{\phi}{2}}{\left[(\omega - \epsilon)^2 - \omega_0^2 \right]^2 + \gamma^2 (\omega - \epsilon)^2} \\
&= \frac{\cos \frac{\phi}{2}}{2\pi} \left[\gamma_+ \left\{ \tan^{-1} \left(\frac{\mu_L - \epsilon}{\gamma_+} \right) - \tan^{-1} \left(\frac{\mu_R - \epsilon}{\gamma_+} \right) \right\} \right. \\
&\quad \left. - \gamma_- \left\{ \tan^{-1} \left(\frac{\mu_L - \epsilon}{\gamma_-} \right) - \tan^{-1} \left(\frac{\mu_R - \epsilon}{\gamma_-} \right) \right\} \right],
\end{aligned}
\quad (34)
$$

which agrees with known results.[5] Using the NEGF formalism, we could similarly investigate the shot noise in the double-dot AB interferometer.[28]

The transmission function is plotted in Fig. 8 displaying destructive interference pattern for $\phi = \pi$ and a constructive behavior for $\phi = 0$. For $\phi \neq n\pi$, the transmission nullifies exactly at the position of the resonant level.[29] The inset presents the current-voltage characteristics for $\phi = \pi/2$ away from the symmetric point (dashed line) and at the symmetric point (dotted line). We note that the double-step structure (indicating on tunneling dynamics at low bias) disappears in
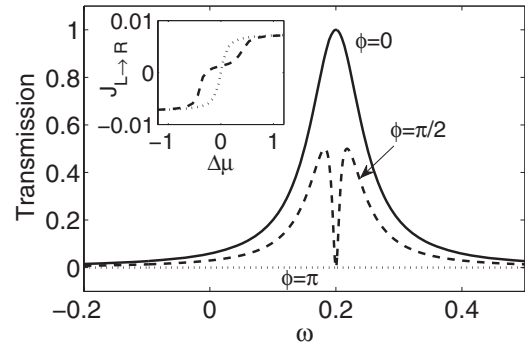
FIG. 8. Transmission coefficient as a function of the energy of an incoming electron, for $\epsilon = 0.2$, $\gamma = 0.05$, $\phi = \pi$ (dotted line), $\phi = \pi/2$ (dashed line), and $\phi = 0$ (full line). The inset presents charge current for $\phi = \pi/2$ and $\epsilon = 0.2$ (dashed line), $\epsilon = 0$ (dotted line).

the latter case. It can be shown that the double-step structure of $\text{Im}\rho_{1,2}$ (see Fig. 7) similarly diminishes at the symmetric point.

IV. TRANSIENT BEHAVIOR

It is of interest to investigate the development of the flux dependency of the occupancy, and the occupancy difference δn, before steady state is reached. Similarly, the dynamics of coherences is nontrivial even without electron-electron interaction effects.[20] We complement the NEGF steady-state expressions of Sec. III with numerical calculations of the transient behavior using an exact numerical tool that is based on the fermionic trace formula[30]

$$\text{Tr}[e^{M_1} e^{M_2} \cdots e^{M_P}] = \det[1 + e^{m_1} e^{m_2} \cdots e^{m_P}]. \quad (35)$$

Here, m_p is a single-particle operator corresponding to a quadratic operator $M_p = \sum_{i,j}(m_p)_{i,j} a_i^\dagger a_j$. $a_i^\dagger$ (a_j) are fermionic creation (annihilation) operators. The trace is performed over all electronic degrees of freedom. Our objective is to study the dynamics of a quadratic operator $B \equiv a_j^\dagger a_k$, $j,k = 1,2$,

$$
\begin{aligned}
\langle B(t) \rangle &= \text{Tr}[\rho_T(t_0) e^{iHt} B e^{-iHt}] \\
&= \lim_{\lambda \to 0} \frac{\partial}{\partial \lambda} \text{Tr}[\rho_L \rho_R \rho e^{iHt} e^{\lambda B} e^{-iHt}]. \quad (36)
\end{aligned}
$$

We introduce the λ parameter, taken to vanish at the end of the calculation. The initial condition is factorized $\rho_T(t_0) = \rho(t_0) \otimes \rho_L \otimes \rho_R$, and these density operators follow an exponential form e^M, with M a quadratic operator. The application of the trace formula leads to

$$
\begin{aligned}
\langle e^{\lambda B(t)} \rangle &= \det\{[I_L - f_L] \otimes [I_R - f_R] \otimes [I_S - f_S] \\
&\quad + e^{iht} e^{\lambda b} e^{-iht} f_L \otimes f_R \otimes f_S\} \quad (37)
\end{aligned}
$$

with b and h as the single-body matrices of the B and H operators, respectively. The matrices I_ν and I_S are the identity matrices for the $\nu = L, R$ space and for the subsystem (dots). The functions f_L and f_R are the band electrons occupancy $f_\nu(\epsilon) = [e^{\beta(\epsilon - \mu_\nu)} + 1]^{-1}$. Here, they are written in matrix form and in the energy representation. f_S represents the initial occupation for the dots, assumed empty, again written
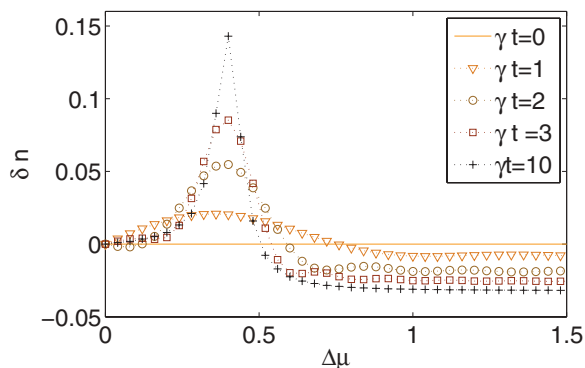
FIG. 9. (Color online) Time evolution of the occupation difference, $\gamma = 0.05$, $\epsilon = 0.2$, $T = 5 \times 10^{-3}$, $\phi = \pi/2$.

in a matrix form. When working with finite-size reservoirs, Eq. (37) can be readily simulated numerically exactly.

Figure 9 displays the evolution of the occupation difference, presented as a function of $\Delta\mu$. In this simulation, we used finite bands with a sharp cutoff $D = \pm 1$. At short time, δn shows weak sensitivity to the actual bias. Only after a certain time, $\gamma t \sim 2$, the peak around the edge at $\Delta\mu = 2\epsilon$ clearly develops. Note that since the band is not very broad, edge effects are reflected at large biases as nonzero occupation difference, in contrast to the broad-bandwidth long-time behavior of Fig. 4.

The transient behavior of the coherences $\mathrm{Re}\rho_{1,2}$ and $\mathrm{Im}\rho_{1,2}$, is included in Fig. 10; the corresponding steady-state values are presented in Fig. 7. We can follow the temporal features of the phase-localization effect, i.e., the disappearance of the real part of the coherence at the symmetric point or at large bias, when $\phi \neq 2\pi n$. Using $\phi = \pi/2$ we note that while at short to intermediate time ($\gamma t < 2$), significant coherence builds up, the real part of the coherence eventually survives only at small biases. Regarding time scales, we find that while $\mathrm{Im}\rho_{1,2}$ reaches the steady-state values at short time $\gamma t \sim 2$, $\mathrm{Re}\rho_{1,2}$ approaches its stationary limit only at longer times, for $\gamma t \sim 10$. Similar results were obtained in Ref. 20.

V. DEPHASING PROBE: STEADY-STATE CHARACTERISTICS

We have discussed so far pure coherent evolution effects in double-dot AB interferometers. It is important to examine at
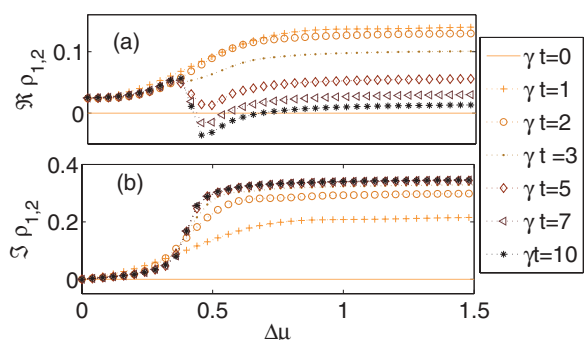
FIG. 10. (Color online) Time evolution of the real (a) and imaginary (b) parts of the coherence using $\gamma = 0.05$, $\epsilon = 0.2$, $T = 5 \times 10^{-3}$, $\phi = \pi/2$.

this point the role of elastic dephasing effects on this evolution as was done experimentally[31,32] and theoretically[33–36] in related systems. Here, we are essentially focused on the effect of dephasing on the modulation of occupation with magnetic flux. Recently, interference and decoherence processes were studied not only in quantum dot structures,[23,24] but in molecular loops as well.[15,16,37,38]

Phase-breaking processes arise due to the interaction of electrons with other degrees of freedom, e.g., with electrons, phonons, and defects. We generalize here the discussion of Sec. III, and incorporate dephasing processes into our system phenomenologically, by using the well-established method of Büttiker dephasing probe.[22] In this technique, elastic dephasing processes on the dots are emulated by including a third terminal P, enforcing the requirement that the charge current towards the probe terminal, at a given electron energy, should vanish. Thus, electrons travel to the probe and return to the system with a different phase, while both electron number and electron energy are conserved. This condition sets an electron distribution within the probe. As we show in the following, away from the symmetric point this distribution effectively depends on the magnetic flux. Other phenomenological tools to incorporate dephasing processes in mesoscopic devices are based on the introduction of random-phase fluctuations into the scattering matrix,[39] or on the inclusion of damping terms into the off-diagonal elements of the density matrix within quantum master-equation (Lindblad or Redfield) formalisms.[40]

Using the Büttiker probe method, we augment the Hamiltonian (1) with a probe, adding to the system a noninteracting electron reservoir P,

$$H_D = H + \sum_{p \in P} \omega_p a_p^\dagger a_p + \sum_{p \in P} \lambda_p a_1^\dagger a_p + \mathrm{H.c.} \quad (38)$$

The parameter λ denotes the coupling strength of dot 1 to the P terminal, taken as a real number. Note that we only allow here for local dephasing on dot 1. One could similarly consider models where both dots are susceptible to dephasing effects, possibly from different sources. Following the equations-of-motion approach as detailed in Sec. III, we arrive at the steady-state expression for the reduced density matrix

$$\langle a_\alpha^\dagger a_\beta \rangle = \frac{1}{2\pi} \sum_{\nu = L, R, P} \int_{-\infty}^{\infty} (G^+ \Gamma^\nu G^-)_{\alpha,\beta} f_\nu(\omega) d\omega. \quad (39)$$

The probe hybridization matrix is given by

$$\Gamma^P = \gamma_P \begin{bmatrix} 1 & 0 \\ 0 & 0 \end{bmatrix}, \quad (40)$$

and the dot's Green's function is written by generalizing the matrix (15), to include the probe self-energy,

$$G^+ = \begin{bmatrix} \omega - \epsilon_1 + \frac{i(\gamma_L + \gamma_R + \gamma_P)}{2} & \frac{i\gamma_L}{2} e^{i\phi/2} + \frac{i\gamma_R}{2} e^{-i\phi/2} \\ \frac{i\gamma_L}{2} e^{-i\phi/2} + \frac{i\gamma_R}{2} e^{i\phi/2} & \omega - \epsilon_2 + \frac{i(\gamma_L + \gamma_R)}{2} \end{bmatrix}^{-1}.$$

This matrix is written here in a general form to allow one to distinguish between the two dots and the different dot-metal hybridization terms. The dot-probe hybridization is defined as $\gamma_P = 2\pi \sum_p |\lambda_p|^2 \delta(\omega - \omega_0)$, in analogy with Eq. (12). In our calculations below we assume energy degenerate dots and symmetric couplings $\epsilon = \epsilon_1 = \epsilon_2$, $\gamma_L = \gamma_R = \gamma/2$.

We now derive the probe distribution by demanding that the energy-resolved charge current to the P terminal vanishes. The total current to P is given by the sum of the currents from the L and R terminals, generalizing Eq. (33):

$$
\begin{aligned}
J_P &= J_{L \to P} + J_{R \to P} \\
&= \frac{1}{2\pi} \int_{-\infty}^{\infty} \mathcal{T}_{LP}(\omega) \left[f_L(\omega) - f_P(\omega) \right] d\omega \\
&\quad + \frac{1}{2\pi} \int_{-\infty}^{\infty} \mathcal{T}_{RP}(\omega) \left[f_R(\omega) - f_P(\omega) \right] d\omega
\end{aligned}
\tag{41}
$$

with the transmission coefficient $\mathcal{T}_{\nu\tilde{\nu}}(\omega) = \mathrm{Tr}[\Gamma^\nu G^+ \Gamma^{\tilde{\nu}} G^-]$. By forcing the integrand to vanish, we arrive at the probe distribution

$$
f_P(\omega) = \frac{\mathcal{T}_{LP}(\omega) f_L(\omega) + \mathcal{T}_{RP}(\omega) f_R(\omega)}{\mathcal{T}_{LP}(\omega) + \mathcal{T}_{RP}(\omega)}.
\tag{42}
$$

Direct evaluation of these transmission coefficients provides the electron distribution in the probe

$$
\begin{aligned}
f_P(\omega) &= \frac{f_L(\omega) + f_R(\omega)}{2} \\
&\quad + \frac{\gamma(\omega - \epsilon) \sin\frac{\phi}{2} \cos\frac{\phi}{2}}{2 \left[(\omega - \epsilon)^2 + \omega_0^2 \right]} \left[f_L(\omega) - f_R(\omega) \right].
\end{aligned}
\tag{43}
$$

As before, $\omega_0 = \frac{\gamma}{2} \sin\frac{\phi}{2}$. This expression indicates that the magnetic flux plays a role in setting the distribution within the probe (such that it only dephases the system and does not deplete electrons or allow energy reorganization). This dependency disappears when the dot energies are set at the symmetric point since the contribution of the second term in Eq. (43) diminishes in the integrals of Eq. (44) from symmetry considerations. We now write integral expressions for the occupation of the dots using Eq. (39):

$$
\begin{aligned}
\rho_{1,1} &= \frac{\gamma}{4\pi} \int_{-\infty}^{\infty} \frac{d\omega}{\Delta(\omega)} \left\{ \left[(\omega - \epsilon)^2 + \omega_0^2 - 2\omega_0(\omega - \epsilon) \cos\frac{\phi}{2} \right] f_L(\omega) + \left[(\omega - \epsilon)^2 + \omega_0^2 + 2\omega_0(\omega - \epsilon) \cos\frac{\phi}{2} \right] f_R(\omega) \right\} \\
&\quad + \frac{\gamma_P}{2\pi} \int_{-\infty}^{\infty} \frac{d\omega}{\Delta(\omega)} \left[(\omega - \epsilon)^2 + \frac{\gamma^2}{4} \right] f_P(\omega), \\
\rho_{2,2} &= \frac{\gamma}{4\pi} \int_{-\infty}^{\infty} \frac{d\omega}{\Delta(\omega)} \left\{ \left[(\omega - \epsilon)^2 + \omega_0^2 + 2\omega_0(\omega - \epsilon) \cos\frac{\phi}{2} + \omega_0\gamma_P \sin\frac{\phi}{2} + \frac{\gamma_P^2}{4} \right] f_L(\omega) \right. \\
&\quad \left. + \left[(\omega - \epsilon)^2 + \omega_0^2 - 2\omega_0(\omega - \epsilon) \cos\frac{\phi}{2} + \omega_0\gamma_P \sin\frac{\phi}{2} + \frac{\gamma_P^2}{4} \right] f_R(\omega) \right\} + \frac{\gamma^2 \gamma_P}{8\pi} \cos^2\frac{\phi}{2} \int_{-\infty}^{\infty} \frac{d\omega}{\Delta(\omega)} f_P(\omega),
\end{aligned}
\tag{44}
$$

with

$$
\Delta(\omega) = \left| (\omega - \epsilon)^2 - \omega_0^2 - \frac{\gamma\gamma_P}{4} + i\left(\gamma + \frac{\gamma_P}{2} \right)(\omega - \epsilon) \right|^2.
$$

In the absence of dephasing, these expressions reduce to Eqs. (18) and (20). In the opposite limit, at very large dephasing $\gamma_P \gg \gamma$, $\gamma_P > \Delta\mu$, we note that $\rho_{2,2}$ is dominated by $\gamma_P^2 \gamma$ terms that are flux independent, while $\rho_{1,1}$ is dominated by its last term $\propto \gamma_P f_P$, which is flux dependent away from the symmetric point, resulting in $\rho_{1,1} \propto \sin(\phi)$. Thus, quite counterintuitively, we find that the level that is directly susceptible to local dephasing demonstrates flux dependency of occupation at strong dephasing, while the level that *indirectly* suffers dephasing effects more feasibly loses its coherent oscillations.

Performing the integration numerically, the dots' occupation and their oscillation with phase are presented in Fig. 11. We observe the following trends upon increasing dephasing strength γ_P: At the symmetric point [Figs. 11(a) and 11(b)], the abrupt jump at zero phase immediately disappears with the application of finite dephasing. When the dot energies are placed away from the symmetric point, yet they buried within the bias window [Figs. 11(c) and 11(d)], the abrupt jump at zero phase again disappears, although the oscillations of occupation with phase prevail until large dephasing $\gamma_P \sim \Delta\mu$. More significantly, when the dot energies are tuned at the edge of the bias window [Figs. 11(e) and 11(f)], we find that

dot 1 (which is directly dephased) develops a new type of oscillation with phase. Only at very large dephasing $\gamma_P \gg \Delta\mu$, these oscillations are overly suppressed. Thus, away from the symmetric point, not only features of coherent dynamics survive even at significant dephasing strength ($\gamma_P \gg \gamma$, $\gamma_P \sim \Delta\mu$), a new type of coherent oscillations may develop as a result of the application of elastic scattering effects on the dots.
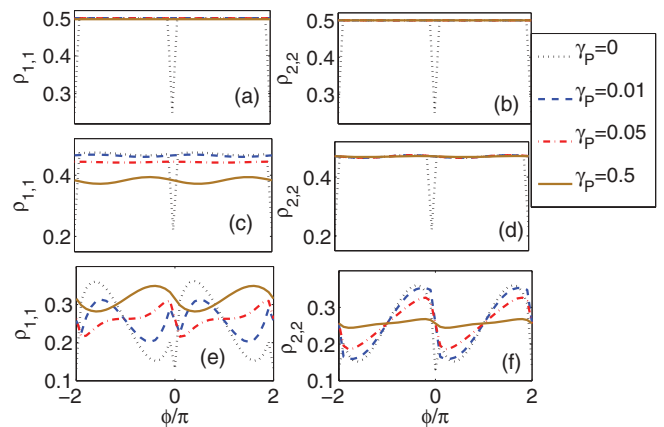
FIG. 11. (Color online) The role of dephasing on the dot occupation–magnetic flux dependency. (a), (b) $\epsilon = 0$, (c), (d) $\epsilon = 0.2$, (e), (f) $\epsilon = 0.3$, where $\gamma_P = 0$ (dotted line), $\gamma_P = 0.01$ (dashed line), $\gamma_P = 0.05$ (dashed-dotted line), and $\gamma_P = 0.5$ (full line). Other parameters are $\gamma = 0.05$, $\Delta\mu = 0.6$, $T = 0$.
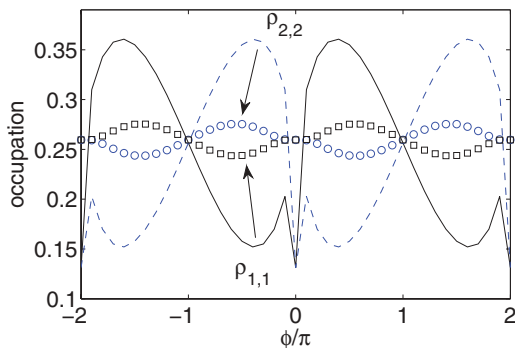
FIG. 12. (Color online) Occupation of the dots in the absence of dephasing (full and dashed lines for dots 1 and 2, respectively), and in the presence of dephasing probes with $\gamma_{P1} = \gamma_{P2} = 0.025$ ($\square$ for $\rho_{1,1}$ and $\circ$ for $\rho_{2,2}$). The arrows indicate that oscillations are systematically suppressed in the indicated direction. We used $\epsilon = 0.3$, $\gamma = 0.05$, $\Delta\mu = 0.6$, $T = 0$.

We can generalize the dephasing model, and study the case with uncorrelated dephasing processes taking place on dots 1 and 2, with dephasing strengths γ_{P1} and γ_{P2}, respectively. Analytic expressions for the occupations of the dots are included in Appendix B. Numerical data are depicted in Fig. 12. We find that coherent oscillations sustain up to $\gamma_{P1}, \gamma_{P2} \sim \gamma$, and finite occupation difference is visible. Since we take the dephasing strengths at each dot to be equal, $\gamma_{P1} = \gamma_{P2}$, the occupation of the dots maintains their relative symmetry. More complicated patterns show when $\gamma_{P1} \neq \gamma_{P2}$. The fact that the model with two dephasing probes provides features distinct from the case with a single probe has been discussed before. For example, in Ref. 41, conductance oscillations for AB rings using different, nonuniform, dephasing around the ring were noted to be distinct.

To conclude, the quantum coherence phenomena discussed in Secs. III and IV should be visible even when dephasing effects take place. Detailed features of, e.g., $\delta n(\phi)$, depend on the way dephasing is applied, whether it is local or uniform. It is interesting to reproduce the behavior observed here while modeling elastic dephasing effects using other techniques.[33–35,39,40]

VI. CONCLUSIONS

In this paper, we have addressed the issue of magnetic-field control on electronic occupation and coherence in a double-dot AB interferometer. The system under investigation included energy degenerate dots with symmetric dot-metals hybridization strengths. However, by voltage gating the dots' levels away from the so-called symmetric point at which $\epsilon = (\mu_L + \mu_R)/2$, we have resolved four nontrivial effects that can allow for significant control over the occupation of quantum dots and their coherence: (i) Occupation may significantly vary with magnetic flux, particularly when the dot level resides close to the bias edge. (ii) The dots acquire different occupations, although they are energy degenerate and the junction is geometrically symmetric. This behavior is maximized at the bias edge $\epsilon \sim \mu_L$. It survives at finite temperature, as long as $T < \gamma$. (iii) Regarding the dots' coherence, we have demonstrated that the effect of "phase localization"[17]

does not take place away from the symmetric point, allowing for decoherence control in the system. Furthermore, (iv) we have found that the system can withstand dephasing processes, to maintain coherent evolution and even develop a new type of oscillations under intermediate dephasing strengths ($\gamma_P \sim \Delta\mu$ and $\gamma_P > \gamma$).

Our minimal model could be applied to describe magnetic-field control in mesoscopic conducting loops and in molecular ring structures. In the latter case it has been noted that degeneracy is crucial for allowing controllability within realistic magnetic-field strengths.[15] Our study has been limited to the noninteracting electron model, excluding both electron-electron interaction effects and other explicit sources for dephasing and inelastic scattering processes. It is of interest to explore the role of interactions on the effects revealed in this paper, as we expect that it would effectively lift the energy degeneracy in the system, further intensifying the effects discussed here. This behavior can be immediately observed at the mean-field level. The Hartree term corrects the dot energies, e.g., $\epsilon_1 \rightarrow \epsilon_1 + U\rho_{2,2}$.[42] Thus, away from the symmetric point, (flux generated) unequal dot occupation translates to effective unequal energetics for the two (identical) dots. Double quantum dots have been proposed as qubits, for implementing quantum computation.[43] The controllability exposed in our study could serve for realizing two-qubit gates and long-lived memory elements.

APPENDIX A: DERIVATION OF EQ. (21)

In this Appendix, we evaluate the following integral analytically:

$$I = \frac{\gamma}{4\pi} \int_{\mu_R}^{\mu_L} d\omega \frac{2\omega_0(\omega - \epsilon)\cos\frac{\phi}{2}}{\left[(\omega - \epsilon)^2 - \omega_0^2\right]^2 + [\gamma(\omega - \epsilon)]^2}. \quad (A1)$$

We achieve this by making use of the following definite integral:

$$I_0 = \int_d^c \frac{x}{(x^2 - a^2)^2 + b^2 x^2} dx$$
$$= \frac{\tan^{-1}\left[\frac{2a^2 - b^2 - 2d^2}{b\sqrt{4a^2 - b^2}}\right] - \tan^{-1}\left[\frac{2a^2 - b^2 - 2c^2}{b\sqrt{4a^2 - b^2}}\right]}{b\sqrt{4a^2 - b^2}}. \quad (A2)$$

In our case, we identify $d = (\mu_R - \epsilon)$, $c = (\mu_L - \epsilon)$, $b = \gamma$, and $a = \frac{\gamma}{2}\sin\frac{\phi}{2}$, leading to $b\sqrt{4a^2 - b^2} = \pm i\gamma^2\cos\frac{\phi}{2}$ and

$$2a^2 - b^2 - 2d^2 = \gamma^2\left[\frac{1}{2}\sin^2\frac{\phi}{2} - 1\right] - 2(\mu_R - \epsilon)^2,$$

$$2a^2 - b^2 - 2c^2 = \gamma^2\left[\frac{1}{2}\sin^2\frac{\phi}{2} - 1\right] - 2(\mu_L - \epsilon)^2.$$

We now reorganize Eq. (A2) using the relations $\tan^{-1} x + \tan^{-1} y = \tan^{-1}(\frac{x+y}{1-xy})$ and $\tan^{-1} z = \frac{i}{2}[\ln(1 - iz) - \ln(1 + iz)]$ to find

$$I_0 = \frac{\ln\left[\frac{F_+(\phi)}{F_-(\phi)}\right]}{2\gamma^2 \cos\frac{\phi}{2}}, \tag{A3}$$

where

$$F_\pm(\phi) = \frac{\gamma^4}{8} \sin^4 \frac{\phi}{2} - (\mu_L - \epsilon)^2 \left[\frac{\gamma^2}{2} \sin^2 \frac{\phi}{2} - (\mu_R - \epsilon)^2 - \gamma^2 \left(1 \pm \cos\frac{\phi}{2}\right)\right]$$
$$- (\mu_R - \epsilon)^2 \left[\frac{\gamma^2}{2} \sin^2 \frac{\phi}{2} - (\mu_L - \epsilon)^2 - \gamma^2 \left(1 \mp \cos\frac{\phi}{2}\right)\right]. \tag{A4}$$

We can reorganize these F functions as a sum of real quadratic terms

$$F_\pm(\phi) = \frac{\gamma^4}{8} \sin^4 \frac{\phi}{2} + 2(\mu_L - \epsilon)^2 (\mu_R - \epsilon)^2 + \frac{\gamma^2}{2}\left(\cos\frac{\phi}{2} \pm 1\right)^2 (\mu_L - \epsilon)^2 + \frac{\gamma^2}{2}\left(\cos\frac{\phi}{2} \mp 1\right)^2 (\mu_R - \epsilon)^2. \tag{A5}$$

Attaching the missing prefactors $I = \frac{\gamma}{4\pi}(2\omega_0) \cos\frac{\phi}{2} \times I_0$, we obtain Eq. (21):

$$I = \frac{\sin\frac{\phi}{2}}{8\pi} \ln\left[\frac{F_+(\phi)}{F_-(\phi)}\right]. \tag{A6}$$

APPENDIX B: OCCUPATION OF THE DOTS WITH TWO INDEPENDENT DEPHASING PROBES

Based on the equation-of-motion approach described in Sec. III, we extend the discussion of Sec. V to include two independent dephasing probes acting on each dot separately. We denote the probe coupled to dot 1 by $P1$, and similarly we identify the probe coupled to dot 2 by $P2$. The elements of the reduced density matrix are given by

$$\langle a_\alpha^\dagger a_\beta \rangle = \frac{1}{2\pi} \sum_\nu \int_{-\infty}^{\infty} (G^+ \Gamma^\nu G^-)_{\alpha,\beta} f_\nu(\omega) d\omega, \tag{B1}$$

and we sum over contributions from all four reservoirs, the electronic baths, and the probes $\nu = L, R, P1, P2$. The probes' hybridization matrices are given by

$$\Gamma^{P1} = \gamma_{P1} \begin{bmatrix} 1 & 0 \\ 0 & 0 \end{bmatrix}, \quad \Gamma^{P2} = \gamma_{P2} \begin{bmatrix} 0 & 0 \\ 0 & 1 \end{bmatrix}. \tag{B2}$$

The dot-metal hybridization matrices and hybridization strengths γ_L and γ_R were included in Sec. III A. It can be shown that the dot's Green's function can be written as

$$G^+ = \begin{bmatrix} \omega - \epsilon_1 + \frac{i(\gamma + \gamma_{P1})}{2} & \frac{i\gamma_L}{2}e^{i\phi/2} + \frac{i\gamma_R}{2}e^{-i\phi/2} \\ \frac{i\gamma_L}{2}e^{-i\phi/2} + \frac{i\gamma_R}{2}e^{i\phi/2} & \omega - \epsilon_2 + \frac{i(\gamma + \gamma_{P2})}{2} \end{bmatrix}^{-1},$$

using $\gamma = \gamma_L + \gamma_R$. We now demand that the energy-resolved current to each probe vanishes, and this condition provides the electron distribution in each probe, given in terms of the transmission functions as in Eq. (42):

$$f_{P1}(\omega) = \frac{f_L(\omega) + f_R(\omega)}{2} + \frac{\gamma(\omega - \epsilon) \sin\frac{\phi}{2} \cos\frac{\phi}{2} [f_L(\omega) - f_R(\omega)]}{2[(\omega - \epsilon)^2 + \omega_0^2 + \gamma_{P2}^2/4 + \omega_0 \gamma_{P2} \sin\frac{\phi}{2}]} \tag{B3}$$

and

$$f_{P2}(\omega) = \frac{f_L(\omega) + f_R(\omega)}{2} - \frac{\gamma(\omega - \epsilon) \sin\frac{\phi}{2} \cos\frac{\phi}{2} [f_L(\omega) - f_R(\omega)]}{2[(\omega - \epsilon)^2 + \omega_0^2 + \gamma_{P1}^2/4 + \omega_0 \gamma_{P1} \sin\frac{\phi}{2}]}. \tag{B4}$$

This expression already assumes degenerate dots $\epsilon_1 = \epsilon_2$. We also used the notation $\omega_0 = \frac{\gamma}{2} \sin \frac{\phi}{2}$. We now return to the reduced density matrix (B1) and substitute these distribution functions to obtain the occupation of dot 1:

$$
\rho_{1,1} = \frac{\gamma}{4\pi} \int_{-\infty}^{\infty} \frac{d\omega}{\Delta(\omega)} \left\{ \left[(\omega - \epsilon)^2 + \omega_0^2 - 2\omega_0(\omega - \epsilon) \cos \frac{\phi}{2} + \gamma_{P2}\omega_0 \sin \frac{\phi}{2} + \frac{\gamma_{P2}^2}{4} \right] f_L(\omega) \right.
$$
$$
+ \left[(\omega - \epsilon)^2 + \omega_0^2 + 2\omega_0(\omega - \epsilon) \cos \frac{\phi}{2} + \gamma_{P2}\omega_0 \sin \frac{\phi}{2} + \frac{\gamma_{P2}^2}{4} \right] f_R(\omega) \right\}
$$
$$
+ \frac{\gamma_{P1}}{2\pi} \int_{-\infty}^{\infty} \frac{d\omega}{\Delta(\omega)} \left[(\omega - \epsilon)^2 + \frac{(\gamma + \gamma_{P2})^2}{4} \right] f_{P1}(\omega) + \frac{\gamma^2 \gamma_{P2}}{8\pi} \cos^2 \frac{\phi}{2} \int_{-\infty}^{\infty} \frac{d\omega}{\Delta(\omega)} f_{P2}(\omega) \tag{B5}
$$

with $\Delta(\omega) = [(\omega - \epsilon)^2 - \omega_0^2 - \frac{1}{4}(\gamma\gamma_{P1} + \gamma\gamma_{P2} + \gamma_{P2}\gamma_{P1})]^2 + (\gamma + \gamma_{P1}/2 + \gamma_{P2}/2)^2(\omega - \epsilon)^2$. An expression for $\rho_{2,2}$ can be similarly written. It is given by Eq. (B5) once we (i) exchange $P1 \leftrightarrow P2$ and (ii) flip signs in front of the $2\omega_0(\omega - \epsilon) \cos \frac{\phi}{2}$ terms.

---

[1] G. Hackenbroich, Phys. Rep. **343**, 463 (2001), and references therein.

[2] Y. Imry, *Introduction to Mesoscopic Physics*, 2nd ed. (Oxford University Press, Oxford, 2002).

[3] A. Yacoby, M. Heiblum, D. Mahalu, and H. Shtrikman, Phys. Rev. Lett. **74**, 4047 (1995).

[4] R. Schuster, E. Buks, M. Heiblum, D. Mahalu, V. Umansky, and H. Shtrikman, Nature (London) **385**, 417 (1997).

[5] J. König and Y. Gefen, Phys. Rev. Lett. **86**, 3855 (2001); Phys. Rev. B **65**, 045316 (2002).

[6] F. Li, X.-Q. Li, W.-M. Zhang, and S. A. Gurvitz, Europhys. Lett. **88**, 37001 (2009).

[7] F. Li, H.-J. Jiao, J.-Y. Luo, X.-Q. Li, S. A. Gurvitz, Phys. E (Amsterdam) **41**, 1707 (2009).

[8] Y. Tokura, H. Nakano, and T. Kubo, New J. Phys. **9**, 113 (2007).

[9] Y.-S. Liu, H. Chen, and X.-F. Yang, J. Phys.: Condens. Matter **19**, 246201 (2007).

[10] D. Boese, W. Hofstetter, and H. Schoeller, Phys. Rev. B **66**, 125315 (2002).

[11] V. Kashcheyevs, A. Schiller, A. Aharony, and O. Entin-Wohlman, Phys. Rev. B **75**, 115313 (2007).

[12] A. Aharony and O. Entin-Wohlman, Phys. Rev. B **72**, 073311 (2005).

[13] O. Hod, E. Rabani, and R. Baer, Acc. Chem. Res. **39**, 109 (2006).

[14] O. Entin-Wohlman and A. Aharony, Phys. Rev. B **85**, 085401 (2012).

[15] D. Rai, O. Hod, and A. Nitzan, J. Phys. Chem. Lett. **2**, 2118 (2011); Phys. Rev. B **85**, 155440 (2012).

[16] D. Rai and M. Galperin, Phys. Rev. B **86**, 045420 (2012).

[17] M. W.-Y. Tu, W.-M. Zhang, and J. Jin, Phys. Rev. B **83**, 115318 (2011).

[18] M. W.-Y. Tu, W.-M. Zhang, J. Jin, O. Entin-Wohlman, and A. Aharony, Phys. Rev. B **86**, 115453 (2012).

[19] M. W.-Y. Tu, W.-M. Zhang, and F. Nori, Phys. Rev. B **86**, 195403 (2012).

[20] S. Bedkihal and D. Segal, Phys. Rev. B **85**, 155324 (2012).

[21] B. Kubala and J. König, Phys. Rev. B **65**, 245301 (2002).

[22] M. Büttiker, Phys. Rev. B **32**, 1846 (1985); **33**, 3020 (1986).

[23] S. Pilgram, P. Samuelsson, H. Förster, and M. Büttiker, Phys. Rev. Lett. **97**, 066801 (2006).

[24] H. Förster, P. Samuelsson, S. Pilgram, and M. Büttiker, Phys. Rev. B **75**, 035340 (2007).

[25] Y. Meir and N. Wingreen, Phys. Rev. Lett. **68**, 2512 (1992).

[26] J. Franson, *Non-Equilibrium Nano-Physics, A Many Body Approach*, Lecture Notes in Physics 809 (Springer, Berlin, 2010).

[27] A. Dhar and D. Sen, Phys. Rev. B **73**, 085119 (2006).

[28] M. Büttiker, Phys. Rev. B **46**, 12485 (1992).

[29] A. Batra, G. Kladnik, H. Vzquez, J. S. Meisner, L. Floreano, C. Nuckolls, D. Cvetko, A. Morgante, and L. Venkataraman, Nat. Commun. **3**, 1086 (2012).

[30] I. Klich, in *Quantum Noise in Mesoscopic Systems*, edited by Yu. V. Nazarov and Ya. M. Blanter (Kluwer, Dordrecht, 2003).

[31] D. Rohrlich, O. Zarchin, M. Heiblum, D. Mahalu, and V. Umansky, Phys. Rev. Lett. **98**, 096803 (2007).

[32] D.-I. Chang, G. L. Khym, K. Kang, Y. Chung, H.-J. Lee, M. Seo, M. Heiblum, D. Mahalu, and V. Umansky, Nat. Phys. **4**, 205 (2008).

[33] A. Ueda and M. Eto, Phys. Rev. B **73**, 235353 (2006); New J. Phys. **9**, 119 (2007); Phys. E (Amsterdam) **40**, 1602 (2008).

[34] Z. Zhu, A. Aharony, O. Entin-Wohlman, and P. C. E. Stamp, Phys. Rev. A **81**, 062127 (2010).

[35] T. Kubo, Y. Tokura, and S. Tarucha, J. Phys. A: Math. Theor. **43**, 354020 (2010).

[36] W. Lai, Y. Xing, and Z. Ma, arXiv:1211.2311.

[37] R. Härtle, M. Butzin, O. Rubio-Pons, and M. Thoss, Phys. Rev. Lett. **107**, 046802 (2011).

[38] S. Ballmann, R. Härtle, P. B. Coto, M. Elbing, M. Mayor, M. R. Bryce, M. Thoss, and H. B. Weber, Phys. Rev. Lett. **109**, 056801 (2012).

[39] M. G. Pala and G. Iannaccone, Phys. Rev. B **69**, 235304 (2004).

[40] H.-P. Breuer and F. Petruccione, *The Theory of Open Quantum Systems* (Oxford University Press, Oxford, UK, 2002).

[41] D. Roy, J. Phys.: Condens. Matter **20**, 025206 (2008).

[42] M. Sindel, A. Silva, Y. Oreg, and J. von Delft, Phys. Rev. B **72**, 125316 (2005).

[43] J. J. L. Morton, D. R. McCamey, M. A. Eriksson, and S. A. Lyon, Nature (London) **479**, 345 (2011).